DOI: 10.1002/ ((please add manuscript number))
Article type: Full paper

2D derivative phase induced growth of 3D all inorganic perovskite micro-nanowire array based photodetectors

Guoqing Tong, Maowei Jiang, Dae-Yong Son, Luis K. Ono and Yabing Qi

Dr. G. Tong, Dr. M. Jiang, Dr. D.-Y. Son, Dr. L. K. Ono and Prof. Y. B. Qi
Energy Materials and Surface Sciences Unit (EMSSU)
Okinawa Institute of Science and Technology Graduate University (OIST)
1919-1 Tancha, Onna-son, Kunigami-gun, Okinawa 904-0495, Japan
*Corresponding author: Yabing Qi, E-mail: Yabing.Qi@OIST.jp

Abstract: A large number of derivative phases in inorganic perovskites have been reported with special structures and shown extraordinary performances in photoelectronic device applications. The reverse phase transition between derivative phases and perovskites usually induces recrystallization or forms mixed components. In this work, we report derivative phase induced growth of the $CsPbBr_3$ micro-nanowire (MW) array by utilizing phase transition of the two-dimensional $CsPb_2Br_5$ phase. Owning to its layered structure and phase transition, annealing of $CsPb_2Br_5$ at a temperature of 550 °C combined with solvent quenching led to a templating effect to form a high-quality CsBr MW array. Subsequent $PbBr_2$ deposition and the second annealing were employed to form the aligned $CsPbBr_3$ MW arrays. Based on this method, a $CsPbBr_3$ MW array based photodetector was fabricated. The large grain size, less grain boundaries (GBs) and lower surface potential of the $CsPbBr_3$ MW array led to high device performance with a responsivity of 7.66 A W^{-1}, a detectivity of ~10^{12} Jones and long-term operational stability over 1900 min.

Introduction

Inorganic halide perovskite materials $CsPbX_3$ (X=Cl, Br and I) have attracted great attention because of their applications in solar cells, light emitting diodes (LEDs), lasers and photodetectors (PDs).[1-4] Their unique properties such as tunable bandgap, high carrier mobility, long carrier diffusion length and high absorption coefficient make them strong candidates for optoelectrical device applications.[5-8] To date, the development of perovskites has evolved from initially three/two-dimensional (3D/2D) bulk films[9,

[10] to low dimensional nano-structures, for example, one-dimensional (1D) nanowires/microwires (NWs/MWs)[11, 12] and zero-dimensional (0D) quantum dots[13, 14].

In comparison with bulk films and quantum dots with many small grains and long-chain ligands, the 1D NWs/MWs exhibit well-aligned structures, lower lateral dimension, less GBs and confined carrier transport in 1D channels/structures, which leads to high crystallinity, less recombination and superior electronic transport behaviors.[15] Additionally, multiple synthesis methods making use of forward growth have been developed such as the solution method[11, 16] (hot-injection,[17] anion exchange[18] etc.) and chemical vapor deposition (CVD).[19, 20] The solution process is a facile, low-cost technique, and has been employed in fabrication of $MAPbI_3$ perovskite nanowires, because of the low synthesis temperature and a precise ratio of precursor materials.[2, 21] However, the existence of residue organic solvents such as DMF, DMSO will affect the quality of perovskites and accelerate the decomposition/degradation of perovskite materials.[22-24] In contrast, the vapor deposition enables high purity of the materials and easy controllability without the adverse effects of residue solvents to ensures long-term stability.[2, 25, 26] In addition, low solubility of all-inorganic perovskites is difficult due to the lower solubility of inorganic perovskites and more complex Cs-Pb-X phase diagram.[21, 23] In parallel, the vapor deposition technique (e.g., all vacuum deposition, CVD) provides a non-solvent environment and high temperature/vacuum system, which allows preparation of highly crystalline NWs without the impurity phase.[21, 27] These strategies have shown ~~showing~~ great advantages in light sources and photodetectors. For example, Wang, Pan and coworkers developed wavelength-tunable in-plane aligned $CsPbX_3$ perovskite NWs lasers with a low pumping threshold of 4 μJ cm^{-2}.[28] Moreover, Meng and coworkers reported a vapor-liquid-solid growth technique to grow high quality $CsPbX_3$ NWs and realized PDs in the visible light regime with an impressive responsivity of 4489 A W^{-1} and detectivity over 7.9×10^{12} Jones.[29] Although perovskite NWs have shown promising performance in optoelectronic devices, random dispersion and short length make it difficult to integrate them into optoelectronic devices. Recently, NW arrays

were proposed to solve this issue because of their controlled alignment and high uniformity in large area. Feng and coworkers reported a 1D $CsPbBr_3$ perovskite NW array based photodetector with a high responsivity exceeding 1000 A W^{-1} by using a micropillar-structured template with asymmetric wettability via the solution method.[11] In addition, Waleed and coworkers reported a vertical $CsPbI_3$ NW array based photodetector with a responsivity of 6.7 mA W^{-1} by combining chemical vapor deposition (CVD) with anodic alumina membrane (AAM) templates.[30] It is worth noting that the formation of NW arrays usually depends on the templates such as AAO/AAM templates[30, 31], CD/DVD disks[32, 33] and photoetching[34] or special substrates like M-template substrates[21, 28] and asymmetric wettability substrates[11, 35]. Use of these templates not only leads to increased cost but also makes it difficult to upscale. A facile and template-free method is desirable for upscaling of NW arrays.

Herein, we propose a two-step method of facile phase induced growth of $CsPbBr_3$ MW arrays by using CsBr as the intermediate product and controlling the decomposition of the $CsPb_2Br_5$ perovskite derivative phase. In the first step, a height of 1.1 μm CsBr MW arrays is obtained by controlling the decomposition from $CsPb_2Br_5$ film ($CsPb_2Br_5 \rightarrow CsBr+2PbBr_2\uparrow$). Then, the CsBr MW arrays are post-treated with extra $PbBr_2$, leading to $CsPbBr_3$ MW arrays with large grain sizes (over 5 μm) and a larger height of 1.72 μm ($CsBr+PbBr_2 \rightarrow CsPbBr_3$). By investigating the growth mechanism of CsBr MW and $CsPbBr_3$ MW arrays, we find that the layered structure of $CsPb_2Br_5$[36] serves as a nominal template, which makes the intermediate product of CsBr MWs possible to grow along the $CsPb_2Br_5$ template to form arrays. Finally, a high-performance photodetector is achieved with an impressive responsivity of 7.66 A W^{-1}, high detectivity of ~10^{12} Jones and long-term operational stability over 1900 min

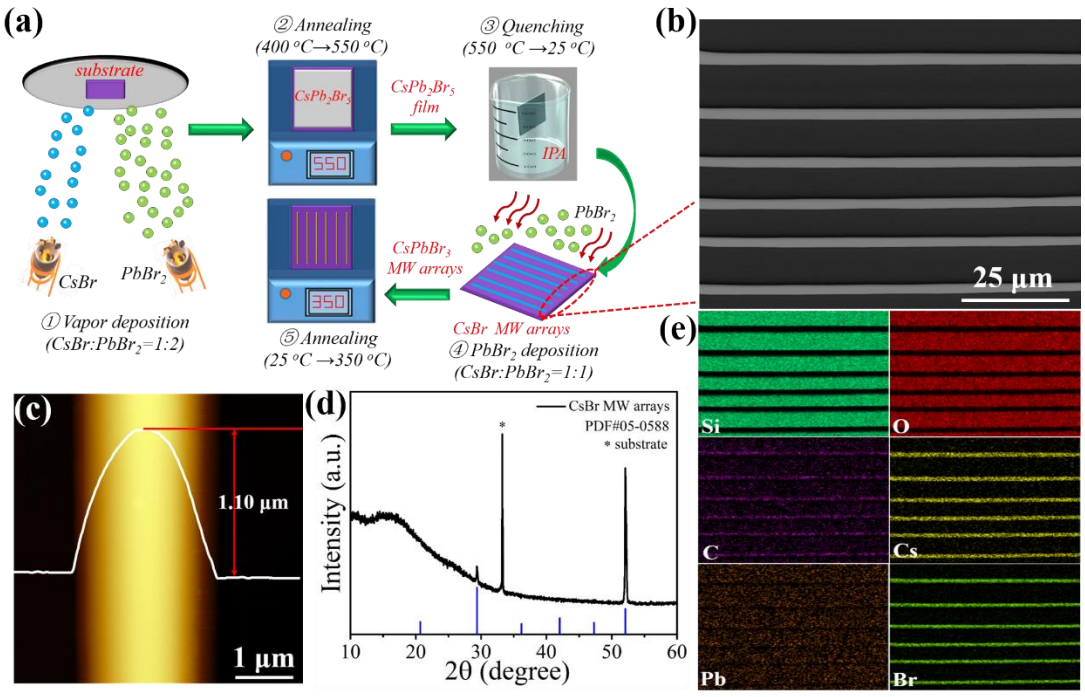

Figure 1. a) Schematic illustration of formation of CsBr MW arrays and $CsPbBr_3$ MW arrays. b) Scanning electron microscope (SEM) image, c) Atomic force microscopy (AFM) morphology image, d) X-ray diffraction pattern (XRD) and e) energy-dispersive X-ray spectroscopy (EDS) mapping of CsBr MW arrays.

Result and discussion

Figure 1a illustrates the growth process of CsBr MW arrays and $CsPbBr_3$ MW arrays. The $CsPb_2Br_5$ precursor layer with a thickness of 1 μm is first deposited on the Si/SiO_2 substrate by a sequential vapor deposition method (more details can be found in Experiment Section). Then the $CsPb_2Br_5$ films are moved to a hotplate (400 °C) rapidly and annealed at a high temperature of 550 °C for 20 min. Solvent quenching is carried out by immersing the samples into an isopropanol (IPA) solution to cool down the samples to room temperature quickly in order to maintain the structure of long MWs. The well-aligned CsBr MW arrays with an average length of ~175 μm can be obtained (**Figure 1b, S1**) as follows: $CsPb_2Br_5 \rightarrow CsBr+2PbBr_2\uparrow$. Notably, energy-dispersive X-ray spectroscopy (EDS) mapping in **Figure 1e**, **S2** shows that Cs and Br are uniformly distributed in the MW arrays. The absence of Pb indicates that $PbBr_2$ has evaporated completely. The Cs:Br composition ratio of 1:1 as seen in the corresponding EDS line scan in **Figure S3, S4** agree well with the stoichiometric ratio of CsBr. The high

crystallinity of the CsBr MW arrays is further confirmed by surface investigation. Atomic force microscopy (AFM) topography images of the CsBr MW arrays and individual MW are shown in **Figure 1c**, **S5**, **S6**. The smooth surface with an average height of 1.1 μm and uniform width of 1~2 μm suggest high crystallinity of the CsBr MWs and MW growth of the CsBr MW array according to Ostwald ripening mechanism during the formation, which will be discussed later. The X-ray diffraction (XRD) pattern in **Figure 1d**, **S7**, **S8** indicates that fabricated CsBr MW arrays exhibit preferred orientation along (211).

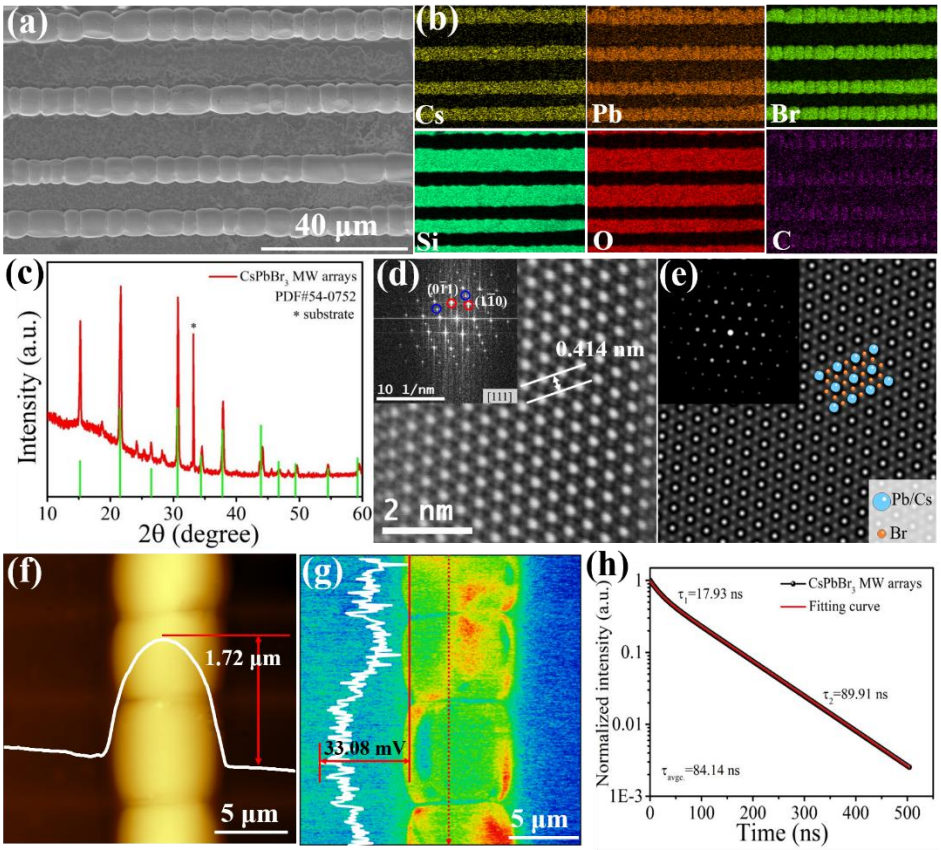

Figure 2. a) SEM image, b) EDS mapping, c) XRD pattern of the $CsPbBr_3$ MW arrays. d) Scanning transmission electron microscopy (STEM) image and e) simulated lattice pattern of the single $CsPbBr_3$ MW. The inset shows the corresponding Fourier transform pattern. f) AFM topography image and g) surface potential distribution of the single $CsPbBr_3$ MW. h) Time resolved photoluminescence (TRPL) decay curve of the $CsPbBr_3$ MW arrays.

Based on the as-synthesized CsBr MW arrays, the $CsPbBr_3$ MW arrays were

obtained (**Figure 2a**) after the post-treatment with an extra $PbBr_2$ film (**Figure S9**) followed by annealing ($CsBr+PbBr_2 \rightarrow CsPbBr_3$), which show uniform distribution and silkworm-like grains. The average grain size is over 5 μm with the maximal size up to 11 μm (**Figure S10**). The EDS element map (**Figure 2b**, **S11**) shows that the MW arrays are composed mainly of the Cs, Pb and Br elements. To extract the precise element ratio, the EDS line scan was performed (**Figure S12**, **S13**) and the corresponding element ratio of Cs, Pb and Br is close to 1:1:3, which agrees well with the stoichiometric ratio of the $CsPbBr_3$ phase. In addition, the absence of Pb and Br in the gap between the MWs (**Figure S14**) indicates that the complete evaporation of extra $PbBr_2$. Furthermore, crystal structure characterization of MW arrays was conducted by XRD. The peaks at 15.19°, 21.55°, 26.48°, 30.64°, 34.37°, 37.77°, 43.89°, 46.69°, 49.38° and 54.51° in **Figure 2c** can be assigned as (100), (110), (111), (200), (210), (211), (220), (300), (310) and (222) diffraction peaks, which indicate that the cubic $CsPbBr_3$ perovskite (**Figure S8**) is formed after the post-treatment by extra $PbBr_2$. Note that $CsPbBr_3$ MW arrays exhibit a polycrystalline structure without oriented growth. To gain more insight into the component and structure of the $CsPbBr_3$ MWs, scanning transmission electron microscopy (STEM) measurements were conducted. The STEM characterization and corresponding simulation images in **Figure 2d, 2e** further demonstrate the crystalline character of $CsPbBr_3$, which is indexed to be the [111] crystal zone of the cubic $CsPbBr_3$ phase. AFM topography images in **Figure 2f**, **S15** illustrate that the $CsPbBr_3$ MW has a height of 1.72 μm and width of MWs is close to 6 μm. Large grain size and high crystallinity of $CsPbBr_3$ grains can effectively reduce recombination at the grain boundaries (GBs). To get a clear comparison with our $CsPbBr_3$ MW arrays, a $CsPbBr_3$ film with a thickness of 1.79 μm was fabricated on the Si/SiO_2 substrates (**Figure S16**). Kelvin probe force microscopy (KPFM) measurements were carried out (**Figure 2g, S17**). In comparison with a conventional $CsPbBr_3$ film that shows an uneven surface potential distribution in the film (**Figure S18**) under light illumination, the $CsPbBr_3$ MW shows a uniform surface potential distribution. This difference can be ascribed to the large and uniform perovskite grain in the MWs, which shows a reduced potential barrier at the GBs and thus is expected to promote carrier transport at GBs as seen in

Figure S17b. In contrast, the uneven grain size distribution indicates that overgrown grains exist in the perovskite film (**Figure S18c**), which can result in carrier accumulation at the GBs because of existence of the potential barrier. Carrier accumulation at GBs would significantly lower the valence and conduction band of the perovskite films as illustrated in **Figure S19**, which induces carrier recombination at the GBs.[37, 38] Furthermore, the steady-state photoluminescence (PL) measurements were carried out for $CsPbBr_3$ MW arrays and films. As seen in **Figure S20**, the enhanced PL intensity of $CsPbBr_3$ MW arrays can be attributed to high quality, less defects and reduced non-radiative recombination in the perovskite grains.[23] The lifetime of charge transport was investigated by time resolved photoluminescence (TRPL). By fitting with the following equation:[39, 40]

$$\tau_{ave} = \frac{A_1\tau_1^2 + A_2\tau_2^2}{A_1\tau_1 + A_2\tau_2}$$

where A_1 and A_2 are the amplitudes, τ_1 and τ_2 represent non-radiative recombination and radiative recombination, respectively. The average lifetime is up to 84.14 ns (**Figure 2h**), which is much longer than the $CsPbBr_3$ film (36.38 ns, **Figure S18d**), indicating that the traps in MWs is effectively suppressed by reducing the GBs and obtaining a large grain size.

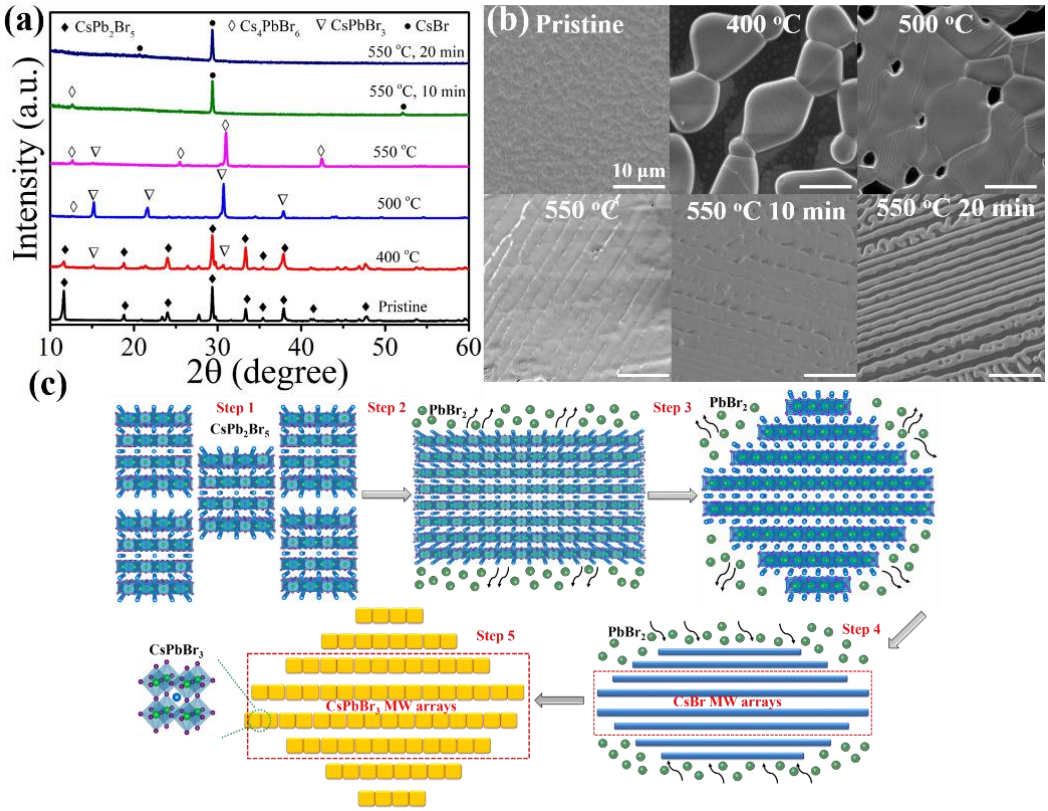

Figure 3. a) XRD patterns and b) corresponding SEM images showing the conversion of the $CsPb_2Br_5$ precursor layer to the CsBr MW array at different temperatures. c) Schematic illustration of formation of the CsBr MW arrays and $CsPbBr_3$ MW arrays.

How to understand the formation of CsBr and $CsPbBr_3$ MW arrays? We first investigated the inverse and forward reactions in $CsPb_2Br_5$. As mentioned above, CsBr reacted with $PbBr_2$ in a molar ratio of 1:2 to form $CsPb_2Br_5$. In contrast, $CsPb_2Br_5$ would easily decompose to $CsPbBr_3$ or CsBr because of the thermal instability at the temperature above 300 °C.[41] As seen in **Figure 3a, 3b**, the pristine $CsPb_2Br_5$ film shows high crystallinity and full coverage (Figure 3b, Pristine). Perovskite grains would quickly melt on the hotplate at 400 °C and grow into large ones in order to reduce the surface energy (Figure 3b). Meanwhile, part of the $CsPb_2Br_5$ phase decomposed to $CsPbBr_3$ with evaporation of $PbBr_2$ because of the low melting point of $PbBr_2$ (357 °C) (Figure 3a, 400 °C).[37] This procedure can be explained by the following equation: $CsPb_2Br_5 \rightarrow CsPbBr_3 + PbBr_2\uparrow$. As the annealing temperature was increased to 500 °C, the grains would grow larger according to the Ostwald ripening mechanism,[42] and

continuously decompose at such a high temperature. Due to the layered structure of $CsPb_2Br_5$, the outmost layers would decompose faster than the inner layers (**Figure 3c**, step 3), which results in stepped structured grains (**Figure 3b**, **S21**, 500 °C). When the treated temperature was further increased to 550 °C, the Cs_4PbBr_6 peaks could be detected in the XRD patterns, which suggests the continuous decomposition of $CsPbBr_3$ follows: $4CsPbBr_3 \rightarrow Cs_4PbBr_6+3PbBr_2 \uparrow$. In addition, the Cs_4PbBr_6 MW arrays (**Figure S22**) could be formed based on the $CsPb_2Br_5$ layer template. Prolonged annealing time (10 min and 20 min) induced the complete disappearance of Cs_4PbBr_6 phase by further extraction of $PbBr_2$ ($Cs_4PbBr_6 \rightarrow 4CsBr + PbBr_2 \uparrow$) and the intermediate products of CsBr MW arrays could be obtained because of the high melting point of CsBr over 660 °C and evaporation of $PbBr_2$ (**Figure 3b** and **3c,** step 4). This decomposition procedure makes the CsBr MW possible to keep the layered structure to construct arrays after fast evaporation of the low melting point component ($PbBr_2$). Although the MWs appeared to grow along a certain direction within a local region of the substrate, on the scale of the whole substrate the MWs grew along different directions. As seen in Figure S1, in this specific sample location, some MWs showed the same orientation along the x direction. However, one of the MWs (Figure S1) was grown along the y direction. To realize the $CsPbBr_3$ MW arrays, extra $PbBr_2$ was deposited on the surface of the CsBr arrays (**Figure S9**). Then the as-prepared samples were annealed at a temperature of 350 °C for 30 min to ensure the further reaction between CsBr and $PbBr_2$ to form highly crystalline $CsPbBr_3$. Finally, silkworm-like $CsPbBr_3$ MWs were obtained with an average grain size about 5 μm.

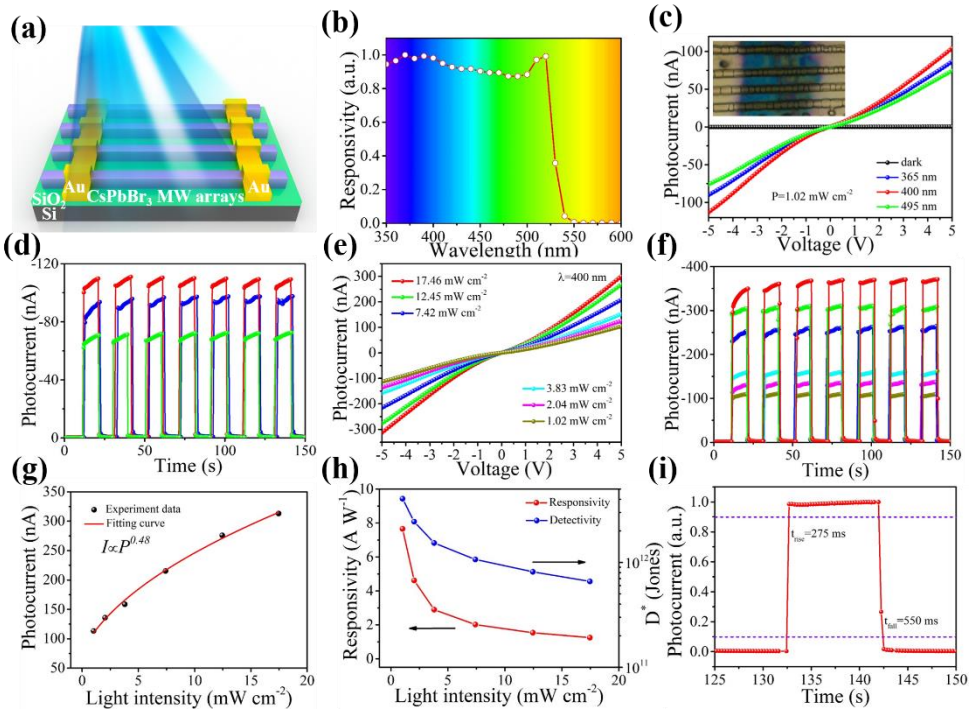

Figure 4. a) Schematic illustration and b) responsivity spectrum of the $CsPbBr_3$ MW arrays photodetector. c) I-V and d) I-t curves of the $CsPbBr_3$ MW array based photodetector under dark and light illumination with different wavelengths. The inset is a photograph of the device. e) I-V and f) I-t curves of the $CsPbBr_3$ MW array based photodetector under light illumination with a wavelength of 400 nm with different power intensities. g) Photocurrent and h) responsivity/detectivity of the device as a function of incident power intensities. i) Response time of the photodetector during one cycle.

The $CsPbBr_3$ MW array based PDs (**Figure 4a**) were fabricated by coating 80 nm gold as the electrode using an aperture mask of 60 μm (**Figure 4c**, inset). The responsivity spectrum of the device (**Figure 4b**) shows a high photoresponsivity in the visible region, which is consistent with the absorption spectrum of $CsPbBr_3$ in our previous works.[7, 37] The current-voltage (I-V) curves in **Figure 4c** show a low dark current of -1.59×10^{-10} A at a bias voltage of -5 V and photocurrent at a fixed power intensity of 1.2 mW cm^{-2} under light illumination with different wavelengths. The high photocurrent of -113.20 nA was achieved at a bias voltage of -5 V under light illumination with a wavelength of 400 nm, which was much higher than the same thickness of $CsPbBr_3$ film photodetector (-50.76 nA, **Figure S23**). In parallel, the photocurrent under illumination light of 365 nm and 450 nm are -90.14 nA and -76.06 nA, respectively. The responsivity (R) and detectivity (D^*) of the PDs were extracted

from the following equations:[43-45]

$$R = \frac{\Delta I}{P_\lambda S} \quad (1)$$

$$D^* = R\sqrt{\frac{S}{2qI_{dark}}} = \frac{R\sqrt{BS}}{i_n} \quad (2)$$

where ΔI is photocurrent ($\Delta I = I_{light} - I_{dark}$, I_{light} and I_{dark} are the current with light illumination and in dark, respectively). P_λ is the light illumination power intensity on the device and S is the active area of the device; q, B and i_n are the elementary charge, electrical bandwidth of noise measurement and noise current, respectively. The $CsPbBr_3$ MW arrays can be regarded as a rectangular-shaped structure and the corresponding active area is estimated as follows:[29] S = n×a×b, where n is the number of MWs in the device (n=4), and a and b are the width of the MWs (6 μm) and length of the channel (60 μm), respectively. The corresponding responsivity/detectivity of the devices under light illumination of 365 nm, 400 nm and 450 nm were 6.13 A W^{-1}/3.25×10^{12} Jones, 7.66 A W^{-1}/4.05×10^{12} Jones and 5.18 A W^{-1}/2.74×10^{12} Jones, respectively. Time-dependent curves (I-t) in **Figure 4d** suggest that high repeatability of the devices under light illumination with different wavelengths. Moreover, the intensity dependent properties of the devices were also investigated by changing the irradiation power intensity from 1.02 to 17.46 mW cm^{-2}. As the incident power intensity increased, the photocurrent of the device was greatly increased (**Figure 4d**) because more carriers were excited and separated. The corresponding I-t curves in **Figure 4e** also exhibited excellent reproducibility even at high power intensity. By fitting the curve in **Figure 4f** with the formula of $I=P^\theta$, where I, P and θ are the photocurrent, power intensity and proportionality constant, respectively, we found that θ was 0.48 for 400 nm incident light, which was not close to the ideal value of 1 because θ was related to recombination processes of photo-generated carriers.[46, 47] This suggests that some traps and recombination centers exist in the device when the devices are operated under a high incident light intensity, but the devices still exhibit a good linearity for photo-detection.[46, 48] In addition, we also conducted the light power intensity investigation at 365 nm and 450 nm in **Figure S24, S25**, which also exhibits an excellent dependence on the power intensity with a good fitting showing a linearity relationship for light

detection. **Figure S26** depicts the response characteristic under different operational biases from -1 V to -5 V, as the corresponding photocurrent increased from 14.4 nA to 367.1 nA, which indicates that the devices could work well under even low bias voltages. Beside responsivity and detectivity, the response time is also an important parameter for photodetectors, representing the photo-sensitivity of the device and can be defined as the photocurrent increase from 10% to 90% (t_{rise}) and decrease from 90% to 10% (t_{fall}) of the maximum value.[49] We chose one cycle from Figure 4f. It is clear that the $CsPbBr_3$ MW array based PD shows a fast response time of 275/550 ms during ON/OFF operation under 400 nm (**Figure 4i**).

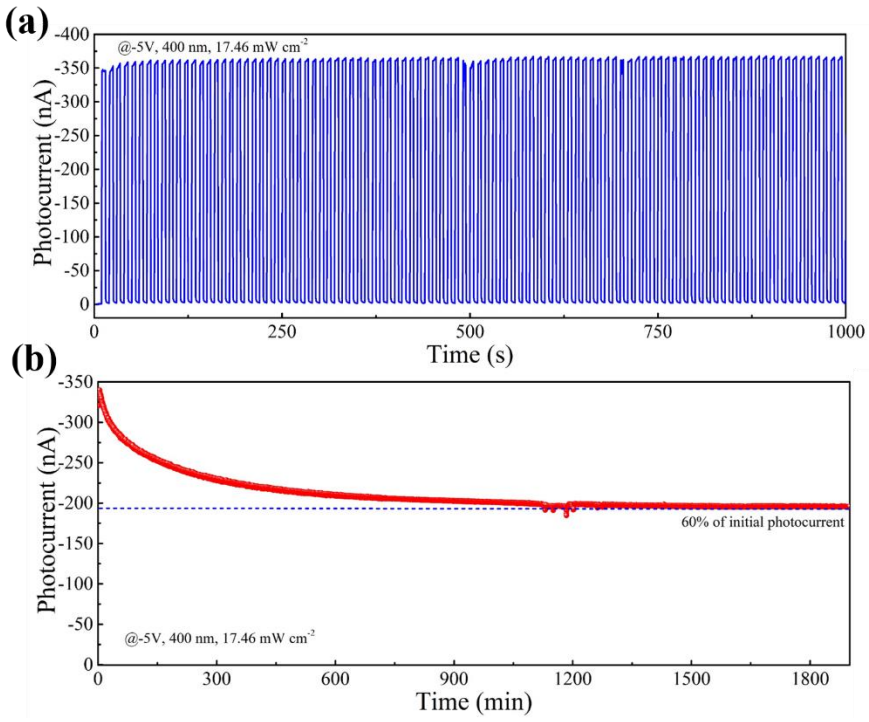

Figure 5. a) Time-dependent response of the $CsPbBr_3$ MW array based PD after 100 cycles of operation. b) Operational stability of $CsPbBr_3$ MW array based PDs under continuous illumination (@400 nm, -5 V, 17.46 mW cm^{-2}).

Furthermore, we also investigated the operational stability of our PD devices. Different from conventional storage stability under dark condition without bias, the operational stability was conducted under continuous light illumination and constant voltage, which reflected the more realistic performance of the PD devices during

operation. First, we switched ON/OFF by repeatedly turning light (400 nm, 17.46 mW cm^{-2}) on and off under a bias voltage of -5 V (**Figure 5a**). The device exhibited excellent reproducibility and stability. After 100 cycles, the photocurrent of the device maintained the same value, which yielded a high ON/OFF ratio of ~10^3. In parallel, continuously light illumination was also performed under 400 nm (~17.46 mW cm^{-2}) at a fixed bias voltage of −5 V. The photocurrent of the device dropped rapidly at the first 600 min and then maintained at a stable value (**Figure 5b**). The devices remained 60% of the initial photocurrent even after 1900 min, which represents better operational stability than previous reports as seen in **Table 1**. The high stability performance can be explained by the improved grain crystallinity, larger grain size (about 5 μm), thicker layer (about 1.72 μm) and fewer grain boundaries. Decomposition/degradation of perovskite devices often starts from the grain boundaries, which serve as a pathway for moisture/oxygen penetration and gradually induce the phase transition/decomposition process toward the grain interiors because chemical binding at grain boundaries with low crystallinity is much weaker than that within the crystal domain interior.[50, 51] On the other hand, charge trapping at the GBs induced by light soaking in the moisture condition can trigger the irreversible degradation of perovskite.[52] In comparison with many GBs in the thin film, high crystallinity and fewer GBs in the $CsPbBr_3$ MW arrays alleviate moisture attacks and charge accumulation at the GBs under long-term illumination under the moisture condition. In parallel, the outmost layer of the thicker $CsPbBr_3$ crystallites in the MW arrays naturally protect the inner crystallites from decomposition/degradation.[50]

Table 1 Comparison of inorganic perovskite nanowires from previous works and this work.

Material	Formation direction	Method	Template	Length (μm)	R (A/W)	D* (Jones)	Operational Stability [min]	Ref
$CsPbBr_3$ MW arrays	**Inverse**	**Vapor**	**No**	**＞200**	**7.66**	**4.05×10^{12}**	**1900**	**This work**
$CsPbBr_3$ NW arrays	Forward	Vapor	No	＜30	—	—	—	[53]
$CsPbBr_3$ NW arrays	Forward	Solution	Yes	＞28	1377	—	—	[11]

$CsPbI_3$ NW nanoarrays	Forward	Vapor	Yes	~10	0.0067	1.5×10^{12}	—	[30]
$CsPbI_3/CsPbBr_3$ NW arrays	Forward	Solution	Yes	＞750	0.125	—	—	[32]
$MAPbI_3$ MW arrays	Forward	Solution	Yes	＞400	13.57	5.25×10^{12}	—	[15]
$MAPbI_3$ NW arrays	Forward	Solution	Yes	＞130	0.012	7.3×10^{12}	10	[33]
$MAPbI_3$ NW arrays	Forward	Solution	No	＞200	4.95	2×10^{13}	—	[54]
$MAPbI_3$ MW arrays	Forward	Solution	No	＞650	0.16	1.3×10^{12}	—	[48]
$MAPbI_3$ NW arrays	Forward	Solution	Yes	＞180	6660	6.85×10^{12}	—	[55]
$MAPb(I_{1-x}Br_x)_3$ NW arrays	Forward	Solution	Yes	＞230	12500	1.73×10^{11}	—	[34]
$FAPbI_3$ NW arrays	Forward	Solution	Yes	＞75	5282	1.45×10^{14}	—	[35]
$CsPbBr_3$ film	Forward	Vapor	—	—	0.375	2.96×10^{11}	—	[45]
$CsPbBr_3$ film	Forward	Solution	—	—	0.010	4.56×10^{8}	—	[56]
$CsPbBr_3$ single crystal	Forward	Solution	—	—	2	—	360	[57]
$CsPbBr_3$ single crystal	Forward	Solution	—	—	0.028	—	—	[58]

※Operational stability is defined as the stability when the device is under a bias voltage and continuous light illumination.

Conclusion

In summary, we reported a 2D derivative phase $CsPb_2Br_5$ induced growth of 3D all inorganic perovskite $CsPbBr_3$ MW arrays. Decomposition of layered structure of 2D $CsPb_2Br_5$ induces the formation of single-crystalline CsBr MW arrays. The CsBr MW arrays are post-treated by extra $PbBr_2$ to convert to $CsPbBr_3$ phase. Impressively, the high performance of a high responsivity of 7.66 A W^{-1} and long-term operational stability over 1900 min are simultaneously realized in the $CsPbBr_3$ MW array photodetectors because of the large grain size, fewer grain boundaries and lower surface potential barrier.

Acknowledgements

This work was supported by funding from the Energy Materials and Surface Sciences Unit of the Okinawa Institute of Science and Technology Graduate University, the OIST R&D Cluster Research Program and the OIST Proof of Concept (POC) Program.

Conflict of Interest

The authors declare no conflict of interest.

Keywords: inorganic perovskite, nanowire arrays, vapor deposition, photodetector, stability

Received: ((will be filled in by the editorial staff))
Revised: ((will be filled in by the editorial staff))
Published online: ((will be filled in by the editorial staff))

References

[1] Q. Tai, K.-C. Tang, F. Yan, *Energy Environ. Sci.* **2019**, *12*, 2375.
[2] X. Zhang, S. Chen, X. Wang, A. Pan, *Small Methods* **2019**, *3*, 1800294.
[3] G. Tong, L. K. Ono, Y. B. Qi, *Energy Technol.* **2020**, *8*, 1900961.
[4] A. Fakharuddin, U. Shabbir, W. Qiu, T. Iqbal, M. Sultan, P. Heremans, L. Schmidt-Mende, *Adv. Mater.* 2019, *31*,1807095.
[5] G. Tong, H. Li, G. Li, T. Zhang, C. Li, L. Yu, J. Xu, Y. Jiang, Y. Shi, K. Chen, *Nano Energy* **2018**, *48*, 536.
[6] J. Zhang, G. Hodes, Z. Jin, S. Liu, *Angew.Chem. Int. Ed.* **2019,** *58*, 2.
[7] G. Tong, T. Chen, H. Li, W. Song, Y. Chang, J. Liu, L. Yu, J. Xu, Y. B. Qi, Y. Jiang, *Sol. RRL* **2019**, *3*, 1900030.
[8] W. Liu, J. Zheng, S. Cao, L. Wang, F. Gao, K.-C. Chou, X. Hou, W. Yang, *Inorg. Chem.* **2018**, *57*, 1598.
[9] H. Tsai, W. Nie, J.-C. Blancon, C. C. Stoumpos, R. Asadpour, B. Harutyunyan, A. J. Neukirch, R. Verduzco, J. J. Crochet, S. Tretiak, L. Pedesseau, J. Even, M. A. Alam, G. Gupta, J. Lou, P. M. Ajayan, M. J. Bedzyk, M. G. Kanatzidis, A. D. Mohit, *Nature* **2016**, *536*, 312.
[10] H. Li , G. Tong, T. Chen, H. Zhu, G. Li, Y. Chang, L. Wang, Y. Jiang, *J. Mater. Chem. A* **2018**, *6*, 14255.
[11] J. Feng, X. Yan, Y. Liu, H. Gao, Y. Wu, B. Su, L. Jiang, *Adv. Mater.* **2017**, *29*, 1605993.

[12] H. Zhou, H. Zhou, S. Yuan, X. Wang, T. Xu, X. Wang, H. Li, W. Zheng, P. Fan, Y. Li, L. Sun, A. Pan, *ACS Nano* **2017**,*11*, 1189.

[13] H.-C. Wang, S.-Y. Lin, A.-C. Tang, B. P. Singh, H.-C. Tong, C.-Y. Chen, Y.-C. Lee, T.-L. Tsai, R.-S. Liu, *Angew.Chem. Int. Ed.* **2016**, *55*, 7924.

[14] M. Jiang, Z. Hu, Z. Liu, Z. Wu, L. K. Ono, Y. B. Qi, *ACS Energy Lett.* **2019**, *4*, 2731.

[15] W. Deng , X. Zhang, L. Huang , X. Xu , L. Wang , J. Wang , Q. Shang , S.-T. Lee , J. Jie, *Adv. Mater.* **2016**, *28*, 2201.

[16] G. Chen, J. Feng, H. Gao, Y. Zhao, Y. Pi, X. Jiang, Y. Wu, L. Jiang, *Adv. Funct. Mater.* **2019**, *29*, 1808741.

[17] T. Yang, Y. Zheng, Z. Du, W. Liu, Z. Yang, F. Gao, L. Wang, K.-C. Chou, X. Hou, W. Yang, *ACS Nano* **2018**, *12*, 1611.

[18] D. Zhang, Y. Yang, Y. Bekenstein, Y. Yu, N. A. Gibson, A. B. Wong, S. W. Eaton, N. Kornienko, Q. Kong, M. Lai, A. P. Alivisatos, S. R. Leone, P. Yang, *J. Am. Chem. Soc.* **2016**, *138*, 7236.

[19] Y. Gao, L. Zhao, Q. Shang, Y. Zhong, Z. Liu, J. Chen, Z. Zhang, J. Shi, W. Du, Y. Zhang, S. Chen, P. Gao, X. Liu, X. Wang, Q. Zhang, *Adv. Mater.* **2018**, *30*, 801805.

[20] J. Chen, Z. Luo, Y. Fu, X. Wang, K. J. Czech, S. Shen, L. Guo, J. C. Wright, A. Pan, S. Jin, *ACS Energy Lett.* **2019**, *4*, 1045.

[21] M. Shoaib, X. Zhang, X. Wang, H. Zhou, T. Xu, X. Wang, X. Hu, H. Liu, X. Fan, W. Zheng, T. Yang, S. Yang, Q. Zhang, X. Zhu, L. Sun, A. Pan, *J. Am. Chem. Soc.* **2017**, *139*, 15592.

[22] Q. Chen, H. Zhou, Z. Hong, S. Luo, H.-S. Duan, H.-H. Wang, Y. Liu, Gang Li, Y. Yang, *J. Am. Chem. Soc.* **2014**, *136*, 622.

[23] G. Tong, M. Jiang, D.-Y. Son, L. Qiu, Z. Liu, L. K. Ono, Y. B. Qi, *ACS Appl. Mater. Interfaces* **2020**, 12, 14185.

[24] H. Kim, K.-G. Lim, T.-W. Lee, *Energy Environ. Sci.* **2016**, *9*, 12.

[25] G. Tong, X. Lan, Z. Song, G. Li, H. Li, L. Yu b, J. Xu, Y. Jiang, Y. Sheng, Yi Shi, K. Chen, *Mater. Today Energy* **2017**, *5*, 173.

[26] B.-S. Kim, M.-H. Choi, M.-S. Choi, J.-J. Kim, *J. Mater. Chem. A* **2016**, *4*, 5663.

[27] J. Chen, Y. Fu, L. Samad, L. Dang, Y. Zhao, S. Shen, L. Guo, S. Jin, *Nano Lett.* **2017**, *17*, 460.

[28] X. Wang, M. Shoaib, X. Wang, X. Zhang, M. He, Z. Luo, W. Zheng, H. Li, T. Yang, X. Zhu, L. Ma, A. Pan, *ACS Nano* **2018**, *12*, 6170.

[29] Y. Meng, C. Lan, F. Li, S. Yip, R. Wei, X. Kang, X. Bu, R. Dong, H. Zhang, J. C. Ho, *ACS Nano* **2019**, *13*, 6060.

[30] A. Waleed, M. M. Tavakoli, L. Gu, S. Hussain, D. Zhang, S. Poddar, Z. Wang, R. Zhang, Z. Fan, *Nano Lett.* **2017**, *17*, 4951.

[31] C.-H. Lin, C.-Y. Kang, T.-Z. Wu, C.-L. Tsai, C.-W. Sher, X. Guan, P.-T. Lee, T. Wu, C.-H. Ho, H.-C. Kuo, J.-H. He. *Adv. Funct. Mater.* **2020**, *30*, 1909275.

[32] M. Wang, W. Tian, F. Cao, M. Wang, L. Li, *Adv. Funct. Mater.* **2020,** DOI: 10.1002/adfm.201909771.

[33] F. Cao, W. Tian, M. Wang, H. Cao, L. Li, *Adv. Funct. Mater.* **2019**, *29*, 1901280.

[34] W. Deng, L. Huang, X. Xu, X. Zhang, X. Jin, S.-T. Lee, J. Jie, *Nano Lett.* **2017**, *17*, 2482.
[35] G. Chen, Y. Qiu, H. Gao, Y. Zhao, J. Feng, L. Jiang, Y. Wu, *Adv. Funct. Mater.* **2020**, DOI: 10.1002/adfm.201908894.
[36] G. Li, H. Wang, Z. Zhu, Y. Chang, T. Zhang, Z. Song, Y. Jiang, *Chem. Commun.* **2016**, *52*, 11296.
[37] G. Tong, T. Chen, H. Li, L. Qiu, Z. Liu, Y. Dang, W. Song, L. K.Ono, Y. Jiang, Y. B. Qi, *Nano Energy* **2019**, *65*, 104015.
[38] A. Dymshits, A. Henning, G. Segev, Y. Rosenwaks, L. Etgar, *Sci. Rep.* **2015**, *5*, 8704.
[39] Z. Wu, Z. Liu, Z. Hu, Z. Hawash, L. Qiu, Y. Jiang, L. K. Ono, Y. B. Qi, *Adv. Mater.* **2019**, *31*, 1804284.
[40] T. Chen, G.Tong, E. Xu, H. Li , P. Li, Z. Zhu, J. Tang, Y. B. Qi, Y. Jiang, *J. Mater. Chem. A* **2019**, *7*, 20597.
[41] F. Palazon, S. Dogan, S. Marras, F. Locardi, I. Nelli, P. Rastogi, M. Ferretti, M. Prato, R. Krahne, L. Manna, *J. Phys. Chem. C* **2017**, *121*, 11956.
[42] M. Yang, T. Zhang, P. Schulz, Z. Li, G. Li, D. H. Kim, N. Guo, J. J. Berry, K. Zhu, Y. Zhao, *Nat. Commun.* **2016**, *7*, 12305.
[43] G. Tong, X. Geng, Y. Yu, L. Yu, J. Xu, Y. Jiang, Y. Sheng, Yi. Shia, K. Chen, *RSC Adv.*, **2017**. *7*, 18224.
[44] J. Miao, F. Zhang, *Laser Photonics Rev.* **2019**, *13*, 1800204.
[45] G. Tong, H. Li, D. Li, Z. Zhu, E. Xu, G. Li, L. Yu, J. Xu, Y. Jiang, *Small*, **2018**, *14*, 1702523.
[46] L.-H. Zeng, S.-H. Lin, Z.-J. Li, Z.-X. Zhang, T.-F. Zhang, C. Xie, C.-H. Mak, Y. Chai, S. P. Lau, L.-B. Luo, Y. H. Tsang, *Adv. Funct. Mater.* **2018**, *28*, 1705970.
[47] X. Li , M. Zhu , M. Du , Z. Lv , L. Zhang , Y. Li , Y. Yang , T. Yang , X. Li , K. Wang, H. Zhu, Y. Fang, *Small* **2016**, *12*, 595.
[48] C.-Y. Wu, W. Peng, T. Fang, B. Wang, C. Xie, L. Wang, W.-H. Yang, L.-B. Luo, *Adv. Electron*. *Mater.* **2019**, *5*, 1900135.
[49] G. Tong, H. Li, Z. Zhu, Y. Zhang, L. Yu, J. Xu, Y. Jiang, *J. Phys. Chem. Lett.* **2018**, *9*, 1592.
[50] Z. Liu, L. Qiu, E. J. Juarez-Perez, Z. Hawash, T. Kim, Y. Jiang, Z. Wu, S. R. Raga, L. K. Ono, S. Liu, Y. B. Qi, *Nat. Commun.* **2018**, *9*, 3880.
[51] J. S. Yun, J. Kim, T. Young, R. J. Patterson, D. Kim, J. Seidel, S. Lim, M. A. Green, S. Huang, A. Ho-Baillie, *Adv. Funct. Mater.* **2018**, *28*, 1705363.
[52] N. Ahn, K. Kwak, M. S. Jang, H. Yoon, B. Y. Lee, J.-K. Lee, P. V. Pikhitsa, J. Byun, M. Cho, *Nat. Commun.* **2016**, *7*, 13422.
[52] E. Oksenberg, E. Sanders, R. Popovitz-Biro, L. Houben, E. Joselevich, *Nano Lett*. **2018**, *18*, 424.
[54] L. Gao, K. Zeng, J. Guo, C. Ge, J. Du, Y. Zhao, C. Chen, H. Deng, Y. He, H. Song, G. Niu, J. Tang, *Nano Lett.* **2016**. *16*, 7446.
[55] W. Deng, J. Jie, X. Xu, Y. Xiao, B. Lu, X. Zhang, X. Zhang, *Adv. Mater.* **2020**, DOI: 10.1002/adma.201908340e1908340.
[56] Y. Dong , Y. Gu , Y. Zou, J. Song, L. Xu , J. Li , J. Xue, X. Li , H. Zeng, *Small*

2016, *12* 5622.
[57] J. Song, Q. Cui, J. Li, J. Xu, Y. Wang, L. Xu, J. Xue, Y. Dong, T. Tian, H. Sun, H. Zeng, *Adv. Optical Mater.* **2017**, *5*, 1700157.
[58] J. Ding, S. Du, Z. Zuo, Y. Zhao, H. Cui, X. Zhan, *J. Phys. Chem. C* **2017**, *121*, 4917.

TOC

2D derivative phase induced growth of 3D all inorganic perovskite micro-nanowire array based photodetectors

Guoqing Tong, Maowei Jiang, Dae-Yong Son, Luis K. Ono and Yabing Qi
Energy Materials and Surface Sciences Unit (EMSSU)
Okinawa Institute of Science and Technology Graduate University (OIST)
1919-1 Tancha, Onna-son, Kunigami-gun, Okinawa 904-0495, Japan
*Corresponding author: Yabing Qi, E-mail: Yabing.Qi@OIST.jp

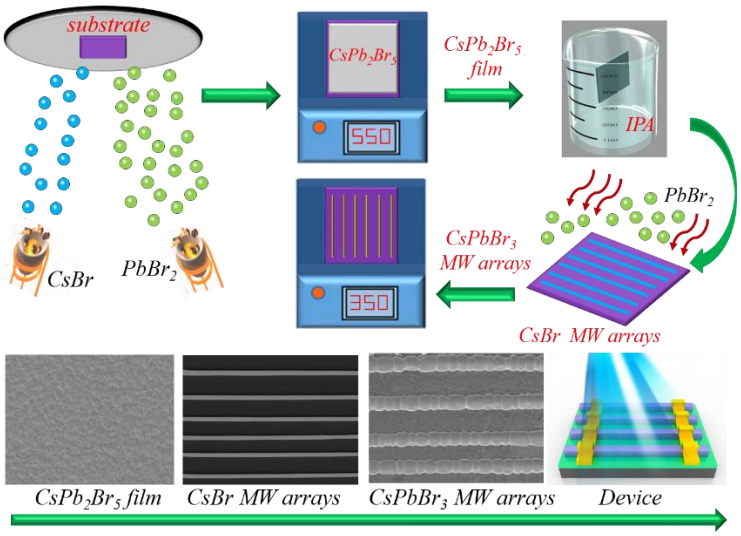

A well aligned $CsPbBr_3$ micro-nanowire (MW) array was synthesized by controlling growth of the intermediate CsBr MW array originated from the deposition of the 2D $CsPb_2Br_5$ phase. Furthermore, a high-performance photodetector was demonstrated based on the $CsPbBr_3$ MW array.